



Cite as
Nano-Micro Lett.
(2026) 18:330

Received: 24 December 2025
Accepted: 23 March 2026
© The Author(s) 2026

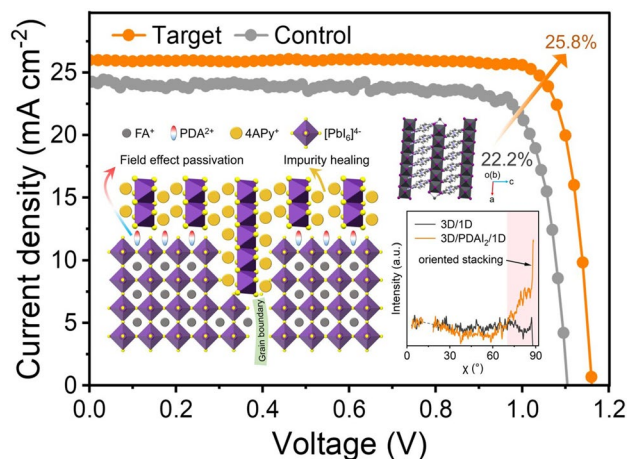
Diamine-Mediated Synergistic Engineering of Orientation and Interfacial Field of 3D/1D Heterojunctions for Efficient Perovskite Photovoltaics

Yaobin Li¹, Yunxuan Cao¹, Yu Zou^{1,2} ✉, Wenjin Yu⁴, Zhenhuang Su⁵, Zhuoer Cai⁶, Yueli Liu¹, Qinyun Liu¹, Hantao Wang¹, Lefan Gong¹, Yucheng Ye¹, Rong Tang¹, Yunan Gao¹, Felix Thomas Eickemeyer⁴, Bo Qu¹ ✉, Lixin Xiao^{1,3} ✉, Zhijian Chen¹ ✉

HIGHLIGHTS

- Constructing 3D/PDAI₂/1D heterojunction through sequential deposition of propane-1,3-diammonium iodide (PDAI₂) and 4APyCl.
- The pre-anchored PDAI₂ not only provides field-effect passivation but also template the subsequent vertical alignment of 1D Pb–I octahedral chains featuring continuous out-of-plane charge transport channels.
- Perovskite solar cells containing 3D/1D structure deliver a champion power conversion efficiency of 25.8% and retain 85% of their initial efficiency after 1000 h maximum power point tracking in accordance with the ISOS-L-1 protocol.

Abstract The performance of three-dimensional (3D) perovskite solar cells (PSCs) is predominantly limited by interfacial non-radiative recombination and instability. Although low-dimensional (LD) interlayers, particularly two-dimensional (2D) perovskites, are widely adopted for surface passivation, their heterogeneous n-values and quantum-well confinement often impede charge transport. One-dimensional (1D) perovskites offer a promising alternative due to their structural flexibility and superior passivation capabilities, yet their potential has been underexploited by challenges in controlled crystallization and ordered orientation. Here, we constructed a 3D/PDAI₂/1D heterojunction through sequential deposition of propane-1,3-diammonium iodide (PDAI₂) and 4-amidinopyridinium chloride (4APyCl). The pre-anchored PDAI₂ not only provides field-effect passivation but also templates the subsequent vertical alignment of 1D Pb–I chains assembled with 4APyCl. This configuration establishes continuous out-of-plane charge transport channels, enabling effective surface defect passivation, favorable energy-level alignment, and enhanced interfacial carrier extraction. The resulting inverted PSCs achieved a champion power conversion efficiency of 25.8% and retained 85% of the initial performance after 1000 h of maximum power point tracking under 1-sun illumination. By demonstrating the critical role of molecular orchestration in LD interlayers, this work provides a blueprint for establishing structure–property relationships and guides the rational design of stable and efficient 3D/1D perovskite photovoltaics.



KEYWORDS Perovskite; Solar cell; 3D/1D heterojunction; Oriented growth; Field effect passivation

Yaobin Li and Yunxuan Cao contributed equally to this work.

✉ Yu Zou, yu.zou@sjtu.edu.cn; Bo Qu, bqu@pku.edu.cn; Lixin Xiao, lxiao@pku.edu.cn; Zhijian Chen, zjchen@pku.edu.cn

¹ State Key Laboratory for Artificial Microstructures and Mesoscopic Physics, School of Physics, Peking University, Beijing 100871, People's Republic of China

Published online: 14 April 2026



SHANGHAI JIAO TONG UNIVERSITY PRESS

Springer

1 Introduction

The photoelectric conversion efficiency (PCE) of three-dimensional (3D) perovskite solar cells (PSCs) has risen from 3.8% in 2008 to nearly 27% currently [1, 2], indicating the significant application prospects of perovskite in the photovoltaic area [3]. In PSCs, the interface between the active layer and the charge transport layer, owing to factors such as numerous defects, lattice mismatch, thermal expansion coefficient mismatch, and energy-level mismatch, can result in severe non-radiative recombination or ion migration, which compromises the device efficiency and stability [4, 5].

Low-dimensional (LD) interfacial layers are extensively employed to passivate surface and grain boundary defects, suppress non-radiative recombination, facilitate energy band matching, and enhance the efficiency and stability of devices [6–9]. Typically, during the solution processing step, the two-dimensional (2D) perovskite layer is formed by spin-coating 2D organic ligands to the surface of 3D perovskite and annealing [10, 11]. A key challenge in practical fabrication is the prevalent formation of mixed 2D perovskite phases, which exhibit discrete n -values and orientations that severely restrict charge transport. This variability imposes stringent demands on achieving controlled crystallization and reproducible processing of 2D perovskites [12]. Further compounding the issue, the discrete $[\text{PbI}_6]^{4-}$ layered framework gives rise to an unfavorable quantum-well structure, thereby limiting the efficiency of interfacial carrier transfer [13–15].

By contrast, one-dimensional (1D) perovskites featuring wire-like Pb–I frameworks exhibit greater structural flexibility and variability, alongside superior passivation capabilities at defect sites like grain boundaries [16–18]. More importantly, unlike the planar 2D counterparts that restrict carrier transport, the spatially more flexible 1D frameworks enable the construction of continuous charge extraction channels, especially when the Pb–I chains are oriented out of plane, thereby optimizing transport efficiency [16, 19]. The advancement of post-solvent rinsing methods has enabled

precise orientation control of low-dimensional perovskites in 3D/2D heterojunctions [13, 14]. Nevertheless, a systematic understanding of how to direct crystallization for achieving uniform and charge-transport-optimized orientations in 1D perovskites remains elusive [20]. Consequently, developing strategies to achieve uniform out-of-plane orientation in 1D perovskites is crucial for harnessing their intrinsic advantages, yet this pivotal bottleneck has often been overlooked, hindering further progress in 3D/1D structured perovskite photovoltaics. Fine-tuning of post-treatment molecular characteristics significantly governs the optoelectronic properties of passivation layers [21]. Previous studies demonstrated that a chlorine-rich environment with suitable cations can promote 1D perovskite formation [22–26]. And organic amidinium cations featuring resonance-enhanced N–H bonds can resist deprotonation and suppress lateral energy landscape inhomogeneity [27–29]. These findings inspired the further design of post-treatment strategies and molecular-level modulation.

Herein, we propose a diamine-mediated synergistic strategy to investigate the influence of diamine ligands in the assembly of 1D perovskites derived from 4APyCl. Upon sequential deposition of propane-1,3-diammonium iodide (PDAI₂) and 4-amidinopyridinium chloride (4APyCl), the pre-deposited PDAI₂ anchors at A-site cation vacancies on the surface while simultaneously serving as field-effect passivation. Subsequently deposited 4APyCl further assembles with residual components such as free PbI₂ to form 1D perovskites. Notably, in contrast to the randomly oriented structures obtained by direct deposition of 4APyCl, the initially adsorbed PDAI₂ guides the vertical alignment of Pb–I octahedral chains and promotes their ordered assembly with 4APyCl to form 1D perovskites, establishing continuous out-of-plane carrier transport channels. Consequently, the integrated 3D/PDAI₂/1D heterojunction exhibits effective healing of surface impurity and defects, along with optimized interfacial electric fields and energy-level alignment, as well as efficient 1D charge transport channels. These synergistic improvements collectively suppress non-radiative

² Future Photovoltaics Research Center, Global Institute of Future Technology (GIFT), Shanghai Jiao Tong University, Shanghai 200240, People's Republic of China

³ AI for Science (AI4S)-Preferred Program, Peking University Shenzhen Graduate School, Shenzhen 518055, People's Republic of China

⁴ Laboratory of Photonics and Interfaces, Institute of Chemical Sciences and Engineering, École Polytechnique Fédérale de Lausanne (EPFL), Lausanne, Switzerland

⁵ Shanghai Synchrotron Radiation Facility (SSRF), Shanghai Advanced Research Institute, Chinese Academy of Sciences, Shanghai 201204, People's Republic of China

⁶ School of Chemistry and Chemical Engineering, Southeast University, Nanjing 211189, People's Republic of China

recombination losses and facilitate enhanced interfacial carrier extraction. The resulting inverted device achieved a champion PCE of 25.8%, ranking it among the top-performing 3D/1D structured perovskite solar cells. Furthermore, reduced impurity and the conformal 1D interfacial capping layer contribute to superior operational stability, enabling unencapsulated devices to retain 85% of their initial PCE after 1000-h operation of continuous 1-sun illumination following the ISOS-L-1 protocol.

2 Experimental Section

2.1 Materials

N,N-Dimethylformamide (DMF, 99.8%), dimethyl sulfoxide (DMSO, 99.9%), methanol (99.9%), ethanol (99.5%), isopropanol (IPA, 99.5%), and chlorobenzene (CB, 99.8%) were purchased from Sigma-Aldrich. [6,6]-Phenyl-C61-butyric acid methyl ester (PCBM, 99.9%) was purchased from Advanced Election Technology Co. [4-(3,6-Dimethyl-9*H*-carbazol-9-yl)butyl]phosphonic acid (Me-4PACz, > 98.0%), 2-(9*H*-carbazol-9-yl)ethylphosphonic acid (2PACz, > 98.0%), and formamidinium iodide (FAI, 99.99%) were purchased from TCI. Methylammonium chloride (MACl, 99.9%), cesium iodide (CsI, 99.999%), lead iodide (PbI₂, 99.99%), lead bromide (PbBr₂, 99.99%), 1,3-propyldiammonium diiodide (PDAI₂, 99.5%), and bathocuproine (BCP, 99%) were purchased from Xi'an Polymer Light Technology Corporation. Methylammonium iodide (MAI, 99.99%) was purchased from Greatcell Solar Materials. 4-Amidinopyridinium chloride (4APyCl, 98%) was purchased from Innochem. All these commercially available materials were used as received without further purification.

2.2 Synthesis of 1D Perovskite (4APy)₂PbI₄

157.6 mg of 4APyCl and 461 mg of PbI₂ were dissolved in 4 mL of DMF. The solution was stirred and dissolved at a temperature of 100 °C or higher, followed by cooling at a rate of 5 °C h⁻¹. This process yielded white needle-like 1D single crystals at the bottom of the vial.

2.3 Device Fabrication

The ITO substrates were ultrasonically cleaned with water, acetone, and IPA for 30 min, respectively. After UV-light treatment for 20 min, the ITO substrates were transferred to N₂ glove box. The Me-4PACz solution (0.33 mg mL⁻¹ dissolved in ethanol) was spin-coated on the ITO substrates at 3000 rpm for 30 s and annealed at 100 °C for 10 min. 1.4 M perovskite precursor solution was prepared by adding FAI, PbI₂, CsI, MAI, MACl, and PbBr₂ into a mixed DMF/DMSO solvent with the ratio of 4:1 following the formula of Cs_{0.05}(FA_{0.95}MA_{0.05})_{0.95}Pb(I_{0.98}Br_{0.02})₃ and stirred until dissolved. Perovskite solutions were deposited by a two-step spin-coating of 1000 rpm for 10 s and 5000 rpm for 30 s. At 15 s before the end of the procedure, 200 μL CB was cast onto the film and annealed at 100 °C for 20 min. For the fabrication of 3D/PDAI₂/1D, the PDAI₂ solution (0.5 mg mL⁻¹ dissolved in a 1:1 mixed solvent of CB and IPA) was spin-coated on the 3D films at 5000 rpm for 30 s and annealed at 100 °C for 5 min. Afterward, the 4APyCl solution (1 mg mL⁻¹ dissolved in IPA) was spin-coated on the 3D/PDAI₂ substrates at 5000 rpm for 30 s and annealed at 80 °C for 5 min. Then, the PCBM solution (20 mg/ml dissolved in CB) was spin-coated at 1500 rpm for 30 s and annealed at 70 °C for 10 min. The saturated supernatant of BCP (dissolved in methanol) was spin-coated at 6000 rpm for 30 s, followed by annealing at 70 °C for 5 min. Finally, 100 nm thickness of Ag was thermally evaporated as an electrode using a shadow mask with aperture area of 0.0672 cm². For devices fabricated on FTO substrates to achieve further efficiency improvement, the ITO substrates were replaced with FTO substrates with anti-reflective coatings, and the solutions of HTL layer were replaced with a mixture of Me-4PACz and 2PACz (0.33 mg mL⁻¹ and 0.17 mg mL⁻¹ in ethanol). All other materials and deposition methods remained unchanged.

2.4 Characterization

The SEM images were characterized by Hitachi S-4800. The XRD patterns were performed by powder X-ray diffractometer (PANalytical) using Cu Kα radiation ($\lambda = 1.5418 \text{ \AA}$) at 40 kV and 40 mA. The XPS spectra and UPS spectra were characterized by Thermo Scientific Nexsa (voltage: 12000.00 V, current: 6 mA, vacuum: $P < 10^{-9}$ mBar, work

FN: 4.20 eV). The steady-state PL and TRPL spectra (excitation at 450 nm) were characterized by FLS1000 (Edinburgh Instruments). The FTIR measurement was characterized by Nicolet iS50 (Thermo Fisher Scientific). The simulated AM 1.5G illumination (100 mW cm^{-2}) sunlight was provided by Newport Thermal Oriel 69911300W solar simulator. Photovoltaic performances of PSCs were measured by Keithley 2611 source meter. GIWAXS was conducted by the BL14B1 beamline at Shanghai Synchrotron Radiation Facility (SSRF). The corresponding X-ray beam possesses a wavelength of 1.24 \AA at a grazing incidence angle of 0.1° and uses an energy of 10 keV. The instruments and parameters used for the measurement and calibration of PLQY are described in the literature [30]. QFLS is derived from PLQY using the following formula: $QFLS = qV_{OC, SQ} + k_B T \ln(PLQY)$, where q is the elementary charge, $V_{OC, SQ}$ is the Shockley–Queisser limit of the open-circuit voltage for the corresponding band-gap, k_B is the Boltzmann constant, and $T = 298.15 \text{ K}$, which is the sample temperature [31]. The AFM and KPFM measurements were characterized by Cypher ES (Oxford Instruments). While measuring each sample, we also measured the potential of a standard sample (ITO). Based on the potential difference and the work function of the standard sample, the surface work function was determined. The EQE spectra were obtained using a QE-R 3011 system (Enlitech, Taiwan) in the range of 300–900 nm. The Mott–Schottky test was characterized by electrochemical workstation (CHI760E, CH Instruments, Inc.) Maximum power point tracking (MPPT) was obtained using a multi-channel solar cell and module stability testing system (MSCLT-1, 91PVKSOLAR).

2.5 Calculation

The Gaussian electrostatic potential of the 4APyCl was calculated in the Gaussian 09 package at the B3LYP/def2TZVP level with DFT-D3 [32].

3 Results and Discussion

3.1 Fabrication of 3D/PDAI₂/1D Heterojunction

For the preparation of the 3D/PDAI₂/1D heterojunction (Fig. 1a), 3D perovskite was initially fabricated on ITO/SAM via a one-step anti-solvent approach. Subsequently, PDAI₂ was deposited to form a field-effect passivation

layer. The molecule features ammonium groups at both ends: One binds to A-site cation vacancies on the surface, and the other induces a surface dipole field that repels holes near the interface [32–35]. Following the spin-coating of 4APyCl, conduct annealing to form a low-dimensional capping layer. The chemical structure of PDAI₂ and 4APyCl is presented in Fig. S1. The molecular structure of 4APyCl exhibits a D-A dipole configuration (Fig. S2). The positive charge is predominantly concentrated on the amine group, whereas the negative charge is mainly localized on the N atom of the pyridine. Synchrotron radiation accelerator-based grazing incidence wide-angle X-ray scattering analysis (GIWAXS) was performed to investigate the impact of the post-treatment of 3D perovskite surfaces [36]. By setting the grazing incidence angle at 0.1° , we were able to acquire the surface information of the post-treated films (Fig. 1b–e). Figure 1f–g presents the out-of-plane (q_z) integration of GIWAXS patterns. On the surface of the 3D perovskite film, a signal of excess PbI₂ can be detected at $q \sim 0.9 \text{ \AA}^{-1}$ [37, 38]. Nevertheless, treatment with either PDAI₂ or 4APyCl can cause the signal of excess PbI₂ to vanish. These two passivating molecules bind to and remove excess PbI₂ impurities, which are known to be detrimental to the stability of perovskite solar cells [39, 40].

After PDAI₂ treatment, no new diffraction rings at lower angles were detected, indicating the absence of low-dimensional structures (Figs. S3 and S4), which is consistent with the findings in the previous literature [33]. However, after treatment with 4APyCl, diffraction rings are observed at $q = 0.58 \text{ \AA}^{-1}$ and $q = 0.69 \text{ \AA}^{-1}$ (Fig. 1d–i). We initially hypothesize that these two inner rings are low-dimensional perovskites formed by the reaction of 4APyCl with PbI₂ (Fig. S5), corresponding specifically to the (002) and (011) crystal planes of a 1D perovskite, as detailed in the next section (Fig. 2). Based on previous research, compared to I[−] anions, the smaller Cl[−] anions further stabilize the 1D phase by increasing its formation energy [23]. We replaced Cl[−] anions with I[−] anions and investigated the XRD patterns of the products from the reaction between 4APyI and PbI₂, as shown in Fig. S6. The reaction of 4APyI with PbI₂ may yields a two-dimensional perovskite, which requires further investigation.

The analysis of the angular dependence of intensity in GIWAXS patterns (intensity- χ) enables the identification of spatial orientation characteristics in crystal structures of

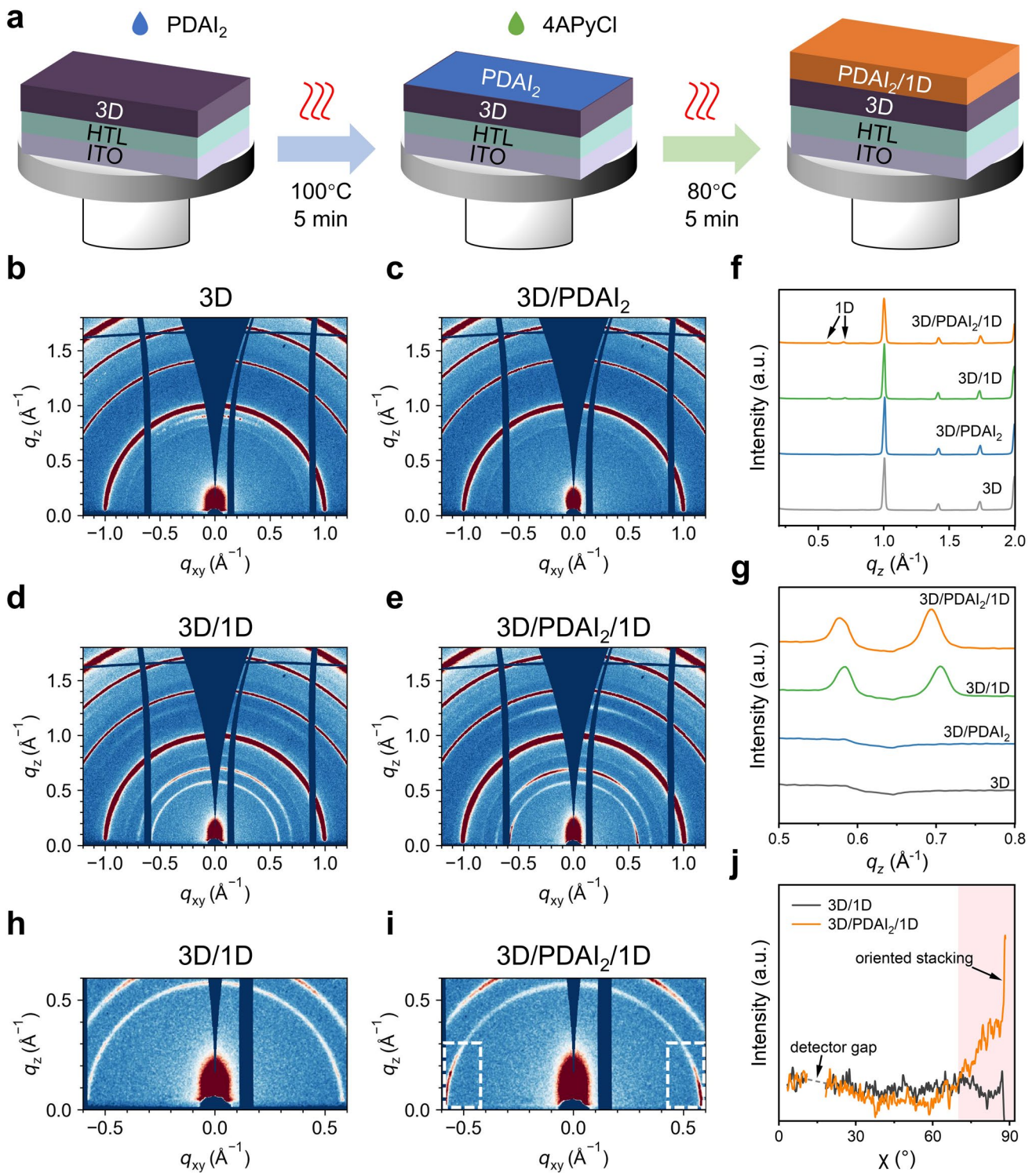


Fig. 1 The fabrication of 3D/PDAI₂/1D heterojunction. **a** Process flow diagram of the fabricating of 3D/PDAI₂/1D heterojunction. GIWAXS images of **b** 3D, **c** 3D/PDAI₂, **d** 3D/1D, and **e** 3D/PDAI₂/1D structured perovskite films. **f**–**g** The GIWAXS intensity profiles near the q_z direction for different samples. Zoom-in view of the GIWAXS patterns near the diffraction ring at $q=0.58$ Å⁻¹ of **h** 3D/1D and **i** 3D/PDAI₂/1D structured films. **j** Intensity- χ plot of the diffraction ring at $q=0.58$ Å⁻¹

1D layer, such as preferential or random orientation [41]. In contrast to the randomly oriented 1D structures obtained through direct deposition of 4APyCl, the 1D structures fabricated via sequential deposition of PDAI₂/4APyCl exhibit ordered orientation (Fig. 1h–i). The diffraction ring of 1D structures at $q = 0.58 \text{ \AA}^{-1}$ demonstrated concentrated high intensity near $\chi \approx \pm 90^\circ$ (as indicated within the white frame, Fig. 1i), confirming a unified preferential in-plane orientation of the 1D perovskite (Fig. 1j), where the Pb–I chains predominantly align perpendicular to the surface of the 3D film along the out-of-plane direction. We propose that, consistent with prior reports [27], the initially deposited PDAI₂ molecules insert and anchor at the A-sites of 3D perovskite surface with their distal ends exposed outward, thereby pre-occupying out-of-plane binding sites. This steric hindrance governs the subsequent binding mode of 4APyCl to the Pb–I framework, guiding its predominantly in-plane alignment and insertion to form bonds that construct vertical Pb–I chains. Consequently, highly oriented 1D perovskite are constructed, featuring Pb–I chains perpendicular to the 3D perovskite surface.

These out-of-plane inorganic chains, together with the field-effect passivation by the pre-deposited PDAI₂, establish a multifunctional surface modulation layer.

Consistent with the elimination of the PbI₂ ring in GIWAXS patterns, the scanning electron microscope (SEM) results revealed that the treatment with PDAI₂ and 4APyCl effectively removes the excess PbI₂ (manifested as bright area) on the surface of the 3D perovskite (Fig. S7) [42]. Notably, after the 4APyCl treatment, the grains exhibit flatter and neater (Fig. S8), larger grain size (Fig. S9), and enhanced crystallinity. Among the conditions investigated, the 3D/PDAI₂/1D sample demonstrates the largest average grain size.

3.2 Crystal Structure of 1D Perovskite (4APy)₂PbI₄

To further verify the crystal structure of the 1D perovskites, single crystals were synthesized from a solution of 4APyCl and PbI₂ in DMF using the solution cooling method [22, 43]. The lattice structure was analyzed using single-crystal X-ray diffraction (SCXRD), as depicted in Fig. 2a–c, and the

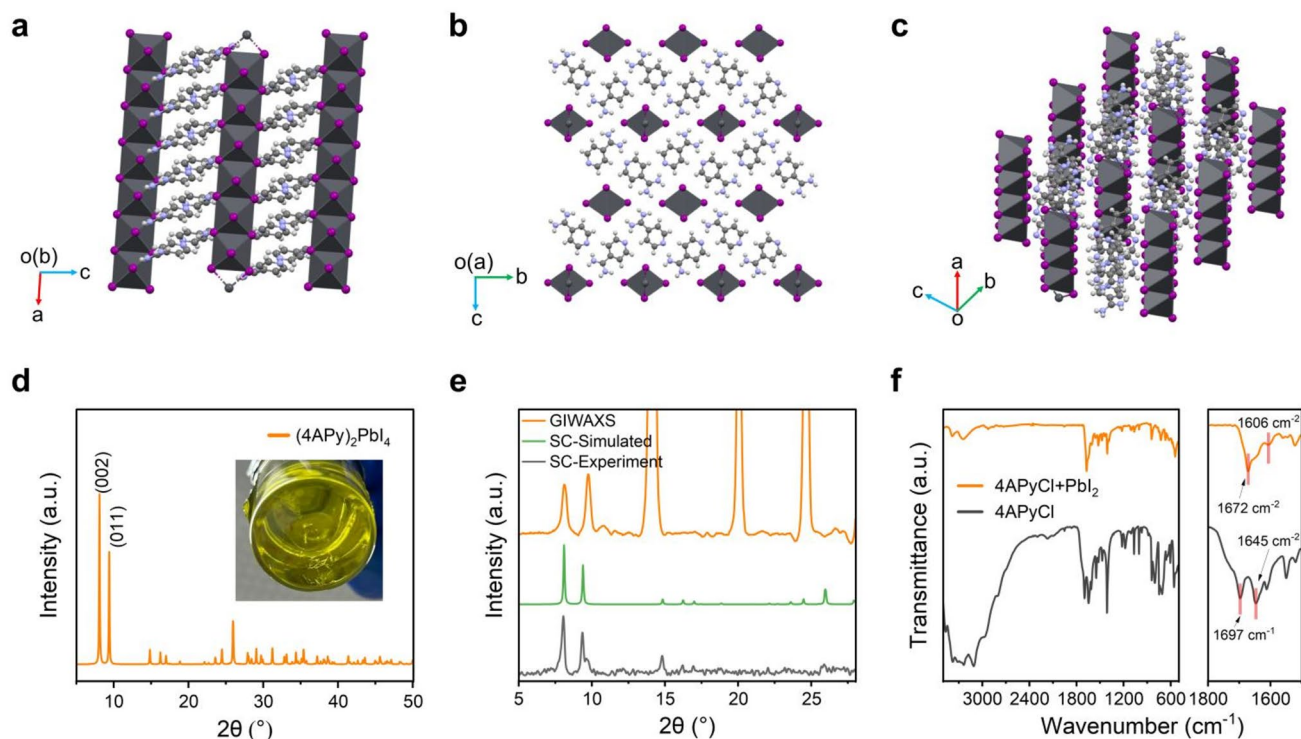


Fig. 2 Crystal structure of 1D perovskite (4APy)₂PbI₄. **a–c** Crystallographic packing diagrams of 1D (4APy)₂PbI₄ perovskites when viewed along different directions. **d** single-crystal XRD patterns for (4APy)₂PbI₄. (Inset) Photograph of a (4APy)₂PbI₄ single crystal. **e** Comparison of experimental and simulated powder XRD patterns for (4APy)₂PbI₄ perovskites, and the GIWAXS intensity profile near the q_z direction for the 3D/PDAI₂/1D structured film. **f** FTIR spectra of 4APyCl and the mixture of 4APyCl and PbI₂

crystal structure parameters are presented in Tables S1 and S2 (CCDC number: 2512007). The edge-shared inorganic Pb–I octahedral chains extend along the *a* direction. In the *b* and *c* directions, large-sized organic cation ligands separate the one-dimensional Pb–I octahedral chains. Accordingly, the grown single crystals are 1D rod-like (Fig. 2d inset). The single-crystal XRD patterns confirms (Fig. 2d) that the Miller indices of the peaks around 8.1° and 9.4° are (002) and (011). We transformed the abscissa q_z of the out-of-plane integration of the GIWAXS pattern of 3D/PDAI₂/1D sample (Fig. 1e) into 2θ and compared it with the experimental and simulated XRD patterns of the one-dimensional perovskite 4APy₂PbI₄ (Fig. 2e). The two peaks in the range of 5°–10° can match well. Therefore, it can be confirmed that when 3D perovskite undergoes post-treatment with 4APyCl, one-dimensional perovskite forms on its surface. Compared to DMF, the use of HI solvent to dissolve PbI₂ and 4APyCl for single-crystal growth yielded larger and higher-quality crystals. The orange crystals obtained correspond to the 2D perovskite 4APyPbI₄, and their XRD results do not match the GIWAXS data of the 3D/4APyCl sample (Figs. S10 and 1d, Note S1). The (002) plane of the 1D perovskite on the surface of 3D/PDAI₂ exhibits a preferential in-plane orientation, whereas the (002) plane of the 1D perovskite on the surface of 3D shows a random orientation. PDAI₂ guides the vertical alignment of Pb–I octahedral chains and promotes their ordered assembly with 4APyCl to form 1D perovskites, establishing continuous out-of-plane carrier transport channels. Consequently, the carriers are not impeded by organic molecules with low conductivity.

Fourier transform infrared spectroscopy (FTIR) results (Fig. 2f) revealed that after mixing with PbI₂, the C=N stretching vibration peak of the FA group of 4APyCl shifts from 1697 to 1672 cm⁻¹, and the C=N stretching vibration peak of the pyridine moiety shifts from 1645 to 1606 cm⁻¹ [44]. We further evaluated the photoelectric characteristics (Fig. S11) of (4APy)₂PbI₄, which showed a photoluminescence (PL) peak at 538 nm, an optical bandgap of 2.77 eV, and a work function of 4.57 eV. Although one-dimensional perovskites exhibit a broader bandgap, the thin-surface passivation layer does not modify the optical bandgap of the perovskite light-absorbing layer (Fig. S12). Additionally, photoelectrical characterizations confirmed the stability of the 1D perovskite polycrystalline thin films in air (Fig. S13).

3.3 Energy-Level Structure of Perovskite Surfaces under Different Passivation Conditions

Kelvin probe force microscopy (KPFM) measurements were employed to characterize the electrical properties of the surfaces of perovskite with different post-treatments (Fig. 3a–d). Consequently, the distribution information of the surface potential and surface work function of the films, along with their average values and the root mean square (R_q), was obtained (Fig. 3e–h). The surface of the 3D perovskite had an average work function of 4.70 eV. After being modified with PDAI₂ on 3D films solely, its work function decreased to 4.61 eV, which could be attributed to the field-effect passivation of PDAI₂ [32]. After modification with 1D on 3D films solely, its work function decreased to 4.64 eV, owing to the electron-donating pyridine groups that increased the surface electron concentration [45]. Under the synergistic effect of the PDAI₂ and 1D passivation, the surface work function decreased to 4.53 eV, with the smallest R_q value of 21.62 meV, indicating the best uniformity of the surface potential. Previous research has indicated that a uniform surface potential is advantageous for enhancing the fill factor (FF) of devices [46]. By measuring the energy band structures of various film surfaces using ultraviolet photoelectron spectroscopy (UPS) (Fig. S14), we were able to obtain the energy band structure diagrams (with the vacuum level unified) (Fig. S15). As depicted in Fig. 3i, the dipole field introduced by PDAI₂ modification coincides with the direction of the built-in electric field in the 3D/electron transport layer (ETL), thus enhancing it and facilitating electron transport. Concurrently, excess PbI₂ impurities are converted into a 1D perovskite capping layer, which exhibits a homogenized morphology and uniform surface potential. The synergistic n-doping effect of PDAI₂ and the 1D perovskite optimizes the energy-level alignment between the modified 3D perovskite and the ETL, thereby collectively facilitating electron extraction and suppressing hole transfer (Fig. 3j).

3D/PDAI₂/1D exhibits the smallest difference between the conduction band energy level (E_C) and the Fermi energy level (E_F). According to Eq. (1) [47]:

$$n = N_C \exp\left(-\frac{E_C - E_F}{k_B T}\right) \quad (1)$$

where N_C is the effective density of states in the conduction band, k_B is the Boltzmann constant, and T is the

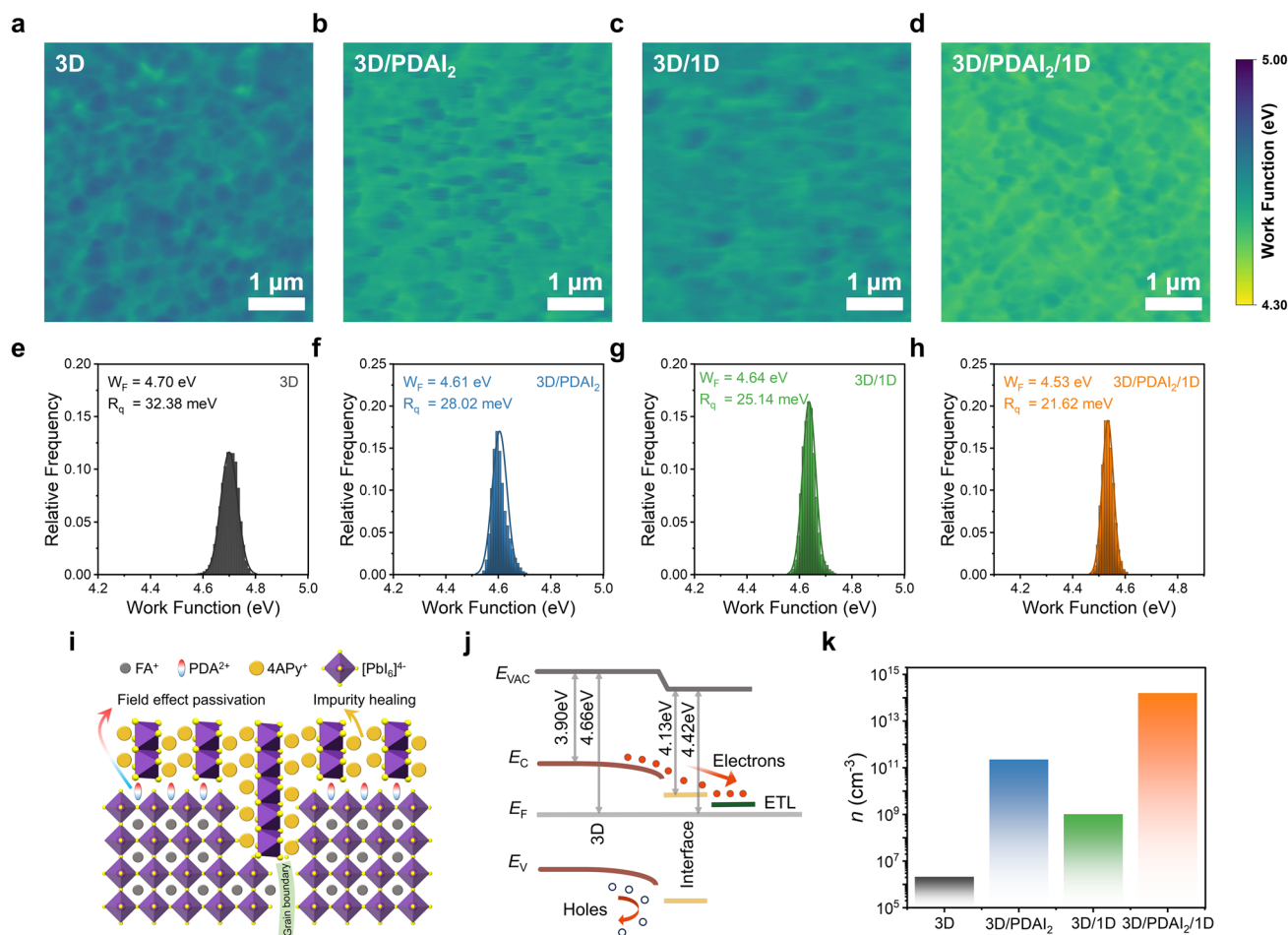


Fig. 3 Energy-level structure of perovskite surfaces under different passivation conditions. KPFM images of **a** 3D, **b** 3D/PDAI₂, **c** 3D/1D, and **d** 3D/PDAI₂/1D perovskite surfaces. **e–h** Statistical distribution of surface work function. **i** Schematic diagram of the surface structure of 3D/PDAI₂/1D. **j** Schematic diagram of the energy-level structure of 3D/PDAI₂/1D heterojunctions. **k** Calculated concentration of electrons in the conduction band

thermodynamic temperature. Through calculation, it can be obtained that the 3D/PDAI₂/1D has the highest surface electron concentration of $1.65 \times 10^{14} \text{ cm}^{-3}$ (Figs. S16 and 3k).

3.4 Photoelectric Properties of Perovskite under Different Post-Passivation Strategies

X-ray photoelectron spectroscopy (XPS) was used to characterize the interactions between passivation molecules and 3D perovskites (Fig. 4a, b). When PDAI₂ was deposited solely on 3D perovskite, there were no significant shifts in the Pb 4*f* peak and I 3*d* peak. However, after depositing the 1D passivation layer, it could be observed that both the Pb 4*f* and I 3*d* peaks shifted toward lower binding energies. The N on the pyridine ring of 4APyCl

acts as an electron donor, increasing the electron density around the Pb and I atoms, enabling the uncoordinated Pb²⁺ defects to be well passivated. Effective defect passivation enables the 3D/1D film to exhibit higher steady-state photoluminescence (PL) intensity and a longer carrier lifetime compared to the 3D film (Fig. 4c, d). The 3D/PDAI₂/1D film, with a more ordered 1D perovskite orientation achieved through the mediation of PDAI₂, can more effectively suppress non-radiative recombination [48]. As a result, it demonstrates the highest PL intensity and the longest carrier lifetime (Table S3). Next, single-electron-carrier devices of perovskite with different structures were constructed to calculate the electron trap state density (n_{trap}). According to the space-charge-limited current (SCLC) method, we can extract the trap-filled limit

voltage (V_{TFL}) from the dark $J-V$ curves of these devices (Fig. 4e), and it is known to satisfy the following Eq. (2):

$$n_{\text{trap}} = \frac{2\epsilon_0\epsilon_r V_{TFL}}{eL^2} \quad (2)$$

where e is the elementary charge, ϵ_0 is vacuum dielectric constant, ϵ_r is relative dielectric constant of perovskite, and L is the thickness of the perovskite film. Based on this formula, the n_{trap} of the 3D/PDAI₂/1D film is calculated to be $1.79 \times 10^{16} \text{ cm}^{-3}$, which is lower than $2.03 \times 10^{16} \text{ cm}^{-3}$ of

the 3D film and $1.92 \times 10^{16} \text{ cm}^{-3}$ of the 3D/1D film. For single-electron-carrier devices, the relationship between J and V satisfies Eq. (3) [49]:

$$J = \frac{9}{8}\epsilon_0\epsilon_r\mu\frac{V^2}{L^3} \quad (3)$$

where J is current density, μ is carrier mobility, and V is voltage applied on devices. By fitting the $J^{1/2}-V$ curves in the child region of the single-carrier devices (Fig. 4f), the electron mobility of the 3D/PDAI₂/1D film can be obtained

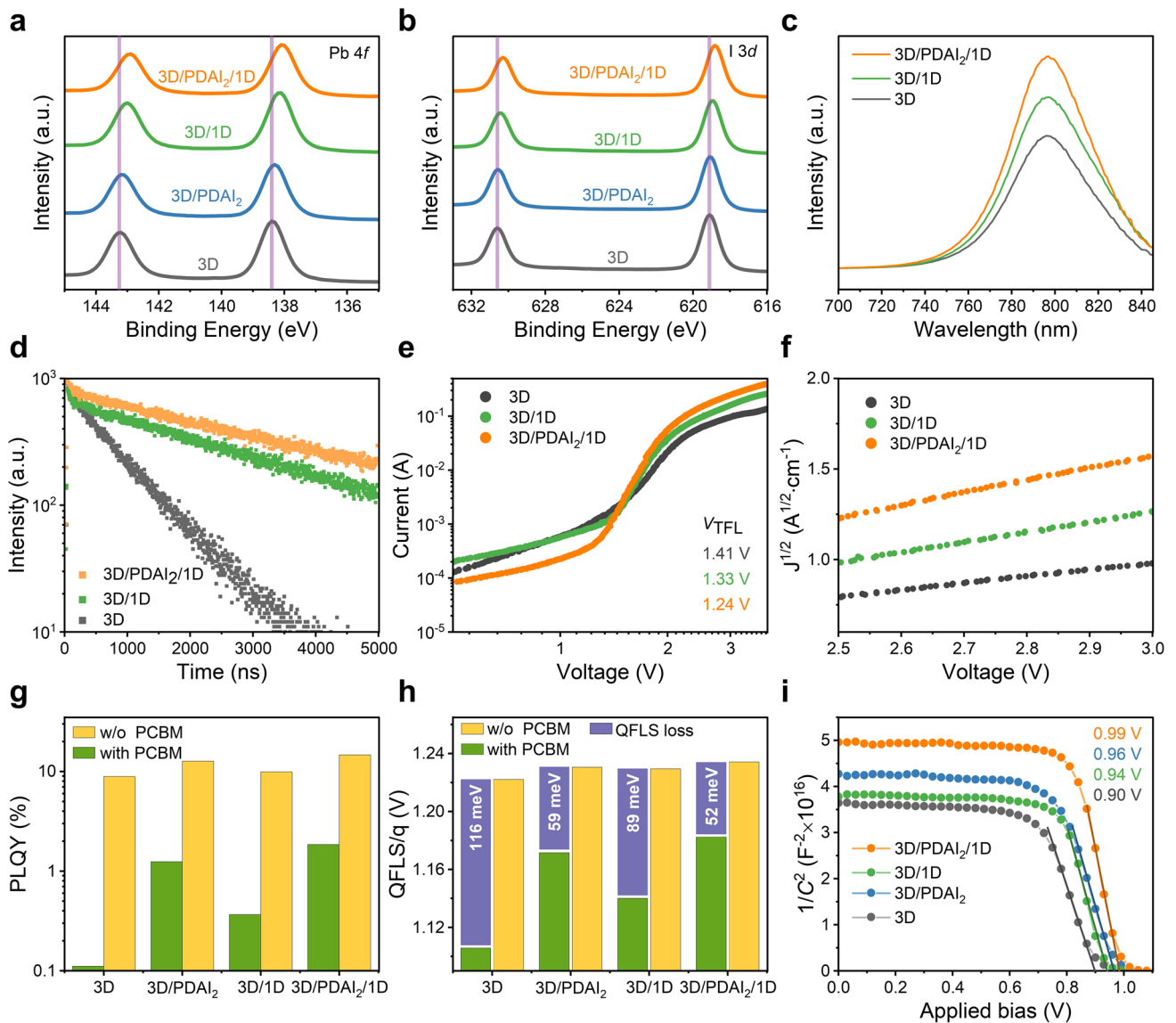


Fig. 4 Photoelectric properties of perovskite under different post-passivation strategies. **a** Pb 4f and **b** I 3d XPS spectra of different perovskite films. **c** Steady-state PL spectra and **d** TRPL spectra of different perovskite films. **e** SCLC plots for single-carrier devices based on the different structured perovskites. **f** $J^{1/2}-V$ curves in the child region of the single-carrier devices. **g** PLQY and **h** QFLS results of perovskite films with different structures, with and without the incorporation of PCBM as the ETL. **i** Mott-Schottky plots of PSCs with different structures

as $2.18 \times 10^{-2} \text{ cm}^2 \text{ V}^{-1} \text{ s}^{-1}$, which is higher than that of the 3D film ($6.65 \times 10^{-3} \text{ cm}^2 \text{ V}^{-1} \text{ s}^{-1}$) and the 3D/1D film ($1.53 \times 10^{-2} \text{ cm}^2 \text{ V}^{-1} \text{ s}^{-1}$).

Furthermore, photoluminescence quantum yield (PLQY) and corresponding quasi-Fermi-level splitting (QFLS) were employed to investigate the mechanisms suppressing defect-assisted carrier recombination losses in the novel heterostructure (Fig. 4g, h). In the absence of the PCBM ETL, the deposition of PDAI₂ and the 1D passivation layer enhanced the QFLS of the perovskite heterojunction compared to bare 3D films, owing to effective passivation of surface impurities by the post-treatment [50, 51]. The 3D/PDAI₂/1D film achieved the highest peak PLQY of 14.67% and a QFLS of 1.234 eV, which is attributed to sufficient chemical passivation enabled by the ordered coverage of the PDAI₂-mediated 1D perovskites. After PCBM deposition, additional interfacial recombination at the perovskite/ETL interface resulted in a reduction in both PLQY and QFLS [52–54]. Notably, the 3D/PDAI₂/1D film exhibited the smallest QFLS loss (52 meV) upon PCBM deposition. This can be ascribed not only to the field-effect passivation capability of PDAI₂ itself, but also to the ordered 1D perovskite channels that promotes efficient carrier separation and transport at the interface [55]. These two effects act synergistically to suppress non-radiative recombination during interfacial charge transfer (Fig. 4g, h). Therefore, the 3D/PDAI₂/1D heterostructure ensures highly efficient carrier transport throughout the entire device, significantly enhancing its performance potential. By performing Mott–Schottky tests on complete solar cell devices, the curves of $1/C^2$ and applied bias voltage V can be obtained (Fig. 4i) and fitted by Eq. (4):

$$\frac{1}{C^2} = \frac{2(V_{\text{bi}} - V)}{A^2 e \epsilon_0 \epsilon_r} \quad (4)$$

where A is the area of the device. The device with the 3D/PDAI₂/1D structure has a built-in electric field of 0.99 V, which is higher than 0.90 V of the 3D device, 0.96 V of the 3D/PDAI₂ device, and 0.94 V of the 3D/1D device. A higher built-in electric field is beneficial for improving the open-circuit voltage (V_{OC}) of the device [56, 57].

3.5 Performance of PSCs Containing Different Structures and Their Stability

We fabricated PSCs with an inverted structure: ITO/[4-(3,6-Dimethyl-9*H*-carbazol-9-yl)butyl]phosphonic acid

(Me-4PACz)/3D/post-treatment layer/PCBM/BCP/Ag (Figs. 5a and S17), and the J – V characteristics of the best-performing PSCs with different post-treatments are shown in Fig. 5b. We found that compared to control PSCs, the 3D/PDAI₂/1D structure led to greatest efficiency improvement (24.3% compared with 22.2%). This can be ascribed to the collective improvement in the V_{OC} (1.102 to 1.167 V), short-circuit current density (J_{SC} , from 24.3 to 25.0 mA cm⁻²), and fill factor (FF) (from 82.9% to 83.3%) (Fig. S18, Table S4) and well in agreement with the EQE spectra and stabilized power output (SPO) data (Figs. S19 and S20). Statistic photovoltaic parameters are summarized in Fig. 5c–e, which demonstrate reproducibility of the performance improvement of PSCs with different post-treatments. V_{OC} increments stem from the improved QFLS and V_{bi} due to the synergistic n-doping of PDAI₂ and 4APyCl, which precisely regulate surface energy levels and reduce interfacial recombination. Meanwhile, the morphological and potential homogenization achieved through 1D passivation contributes to the improvement of FF. At low concentrations, the post-treatment exhibits a relatively weak passivation effect, leading to limited enhancement in V_{OC} . Conversely, higher concentrations impair the device's J_{SC} and FF. Therefore, for the 3D/PDAI₂/1D device, the concentration of PDAI₂ was optimized to 0.5 mg mL⁻¹, while that of 4APyCl was optimized to 1 mg mL⁻¹ (Figs. S21 and S22).

To further validate the application potential of this synergistic surface engineering strategy, we fabricated devices with an FTO/Me-4PACz with 2-(9*H*-carbazol-9-yl)ethyl) phosphonic acid/3D/PDAI₂/1D/PCBM/BCP/Ag structure. Effective light management and interfacial contact within the devices were achieved by utilizing FTO substrates with an anti-reflection coatings. The best-performing device achieved a champion PCE of 25.8% with a V_{OC} of 1.170 V, a J_{SC} of 26.0 mA cm⁻², and an FF of 84.9% (Fig. 5f, Table S5), ranking it among the top-performing 3D/1D structured perovskite solar cells (Fig. 5g, Table S6). To study the effect of PDAI₂/1D capping layer on the stability of PSCs, the unencapsulated devices are subjected to MPPT in accordance with the ISOS-L-1 protocol (Fig. 5h). Reduced impurity and the conformal 1D interfacial capping layer contribute to superior operational stability. Consequently, the device with a 3D/PDAI₂/1D heterostructure retained 85% of its initial PCE after 1000 h of continuous illumination, compared to 64% for its 3D/1D counterpart and a mere 54% for the control device after just 500 h.

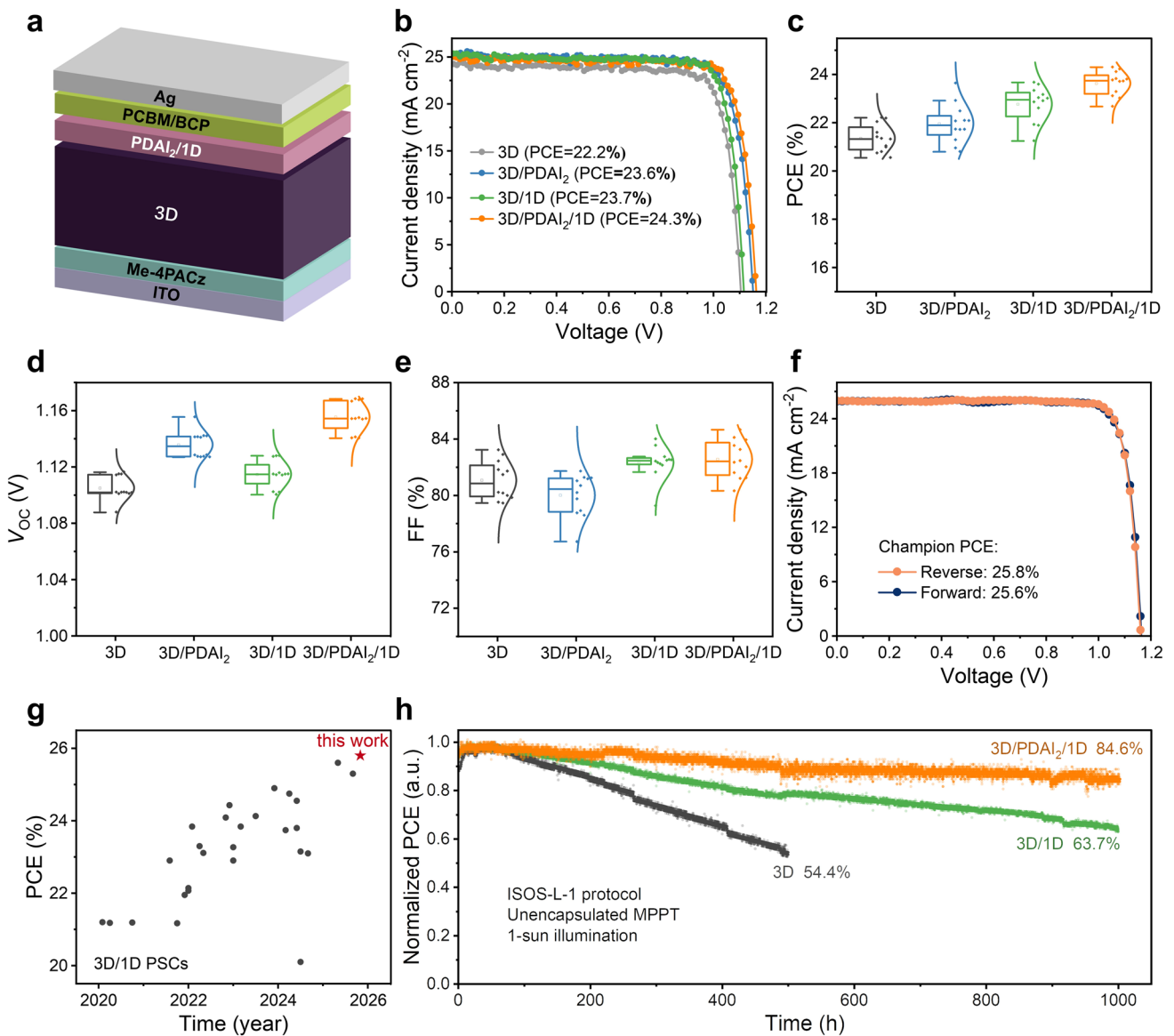


Fig. 5 Performance of PSCs containing different structures and their stability. **a** Diagram of device structure. **b** *J-V* characteristics of the best-performing PSCs with different structure based on the ITO substrates without anti-reflective layer. Box plot of **c** PCE, **d** *V*_{oc}, and **e** FF of PSCs with different structures. **f** *J-V* characteristics of the best-performing 3D/PDAI₂/1D structured PSCs based on the FTO substrates with an anti-reflective layer. **g** Summary of recently reported PSCs based on 3D/1D heterojunctions (PCE > 20%). **h** MPPT of PSCs under continuous 1-sun illumination according to ISOS-L-1 protocol

4 Conclusions

In summary, highly ordered 1D perovskite capping layer was successfully fabricated on 3D/PDAI₂. The pre-anchored PDAI₂ not only provides field-effect passivation but also templates the subsequent vertical alignment of 1D Pb-I octahedral chains featuring continuous out-of-plane charge transport channels. Homogenized morphology and surface

potential are realized through the conversion of excess PbI₂ impurities into low-dimensional capping layer. The synergistic n-doping effect of PDAI₂ and the 4APyCl optimizes the energy-level alignment between the modified 3D perovskite and the ETL, thereby collectively facilitating electron extraction and suppressing hole transfer. Consequently, the corresponding inverted PSCs deliver a champion power conversion efficiency of 25.8% and retain 85% of their initial

efficiency after 1000 h MPPT in accordance with the ISOS-L-1 protocol. This leverages orientation engineering in the 1D perovskite to preserve the impurity healing benefits of the 1D capping layer while avoiding charge transport losses, thus advancing the prospects for fully realizing the potential of 3D/1D heterostructures.

Acknowledgements The authors acknowledge the advisory support from Prof. Dr. Michael Grätzel and also to Laboratory of Photonics and Interfaces, Institute of Chemical Sciences and Engineering, École Polytechnique Fédérale de Lausanne (EPFL). The authors acknowledge the support from the beamline BL14B1 at the Shanghai Synchrotron Radiation Facility (SSRF) for GIWAXS tests. This study was financially supported by the National Key Research and Development Program of China (No. 2022YFB4200500), the National Natural Science Foundation of China (Nos.12174013, 52173153, 62475002, 12574450, 22509126), the Postdoctoral Fellowship Program of CPSF (Grant No. GZB20250060), and the China Postdoctoral Science Foundation (Grant No. 2024M761964).

Author Contributions Y. Li and Y. Zou conceived the idea and designed and conducted the experiment. Y. Cao promoted the project and helped the fabrication of PSCs. W. Yu and Felix T. Eickemeyer contributed to the PLQY and QFLS characterization. Z. Su conducted the GIWAXS experiment. Z. Cai conducted the single-crystal structure analysis. Q. Liu and Y. Gao contributed to the KPFM characterization. Y. Liu, H. Wang, L. Gong, Y. Ye, and R. Tang participated in the data analysis and discussion of the experimental results. Y. Zou, B. Qu, L. Xiao, and Z. Chen supervised the project.

Declarations

Conflict of interest The authors declare no conflict of interest. They have no known competing financial interests or personal relationships that could have appeared to influence the work reported in this paper.

Open Access This article is licensed under a Creative Commons Attribution 4.0 International License, which permits use, sharing, adaptation, distribution and reproduction in any medium or format, as long as you give appropriate credit to the original author(s) and the source, provide a link to the Creative Commons licence, and indicate if changes were made. The images or other third party material in this article are included in the article's Creative Commons licence, unless indicated otherwise in a credit line to the material. If material is not included in the article's Creative Commons licence and your intended use is not permitted by statutory regulation or exceeds the permitted use, you will need to obtain permission directly from the copyright holder. To view a copy of this licence, visit <http://creativecommons.org/licenses/by/4.0/>.

Supplementary Information The online version contains supplementary material available at <https://doi.org/10.1007/s40820-026-02190-z>.

References

1. J. Du, J. Chen, B. Ouyang, A. Sun, C. Tian et al., Face-on oriented self-assembled molecules with enhanced π - π stacking for highly efficient inverted perovskite solar cells on rough FTO substrates. *Energy Environ. Sci.* **18**(7), 3196–3210 (2025). <https://doi.org/10.1039/D4EE05849F>
2. X. Shen, X. Lin, H. Su, Z. Zhang, T. Wu et al., Key advancements and emerging trends of perovskite solar cells in 2024–2025. *Nano-Micro Lett.* **18**(1), 209 (2026). <https://doi.org/10.1007/s40820-025-02022-6>
3. Y. Liu, Z. Zhang, T. Wu, W. Xiang, Z. Qin et al., Cost effectiveness analysis of perovskite solar cells: will it outperform crystalline silicon ones? *Nano-Micro Lett.* **17**(1), 219 (2025). <https://doi.org/10.1007/s40820-025-01744-x>
4. B. Li, S. Li, J. Gong, X. Wu, Z. Li et al., Fundamental understanding of stability for halide perovskite photovoltaics: the importance of interfaces. *Chem* **10**(1), 35–47 (2024). <https://doi.org/10.1016/j.chempr.2023.09.002>
5. H. Lee, T. Moon, Y. Lee, J. Kim, Structural mechanisms of quasi-2D perovskites for next-generation photovoltaics. *Nano-Micro Lett.* **17**(1), 139 (2025). <https://doi.org/10.1007/s40820-024-01609-9>
6. Y. Zhang, J. Xi, Y. Deng, W. Liu, Z. Li et al., The crucial role of organic ligands on 2D/3D perovskite solar cells: a comprehensive review. *Adv. Energy Mater.* **14**(48), 2403326 (2024). <https://doi.org/10.1002/aenm.202403326>
7. Y. Chen, B. Liu, Q. Zhou, D. Ma, X. Han et al., Critical role of 1D materials in realizing efficient and stable perovskite solar cells. *J. Mater. Chem. A* **11**(35), 18592–18604 (2023). <https://doi.org/10.1039/D3TA03174H>
8. H. Rafique, G. Abbas, M.J. Mendes, P. Barquinha, R. Martins et al., Recent advancements and perspectives of low-dimensional halide perovskites for visual perception and optoelectronic applications. *Nano-Micro Lett.* **18**(1), 44 (2025). <https://doi.org/10.1007/s40820-025-01823-z>
9. X. Shen, X. Lin, Y. Peng, Y. Zhang, F. Long et al., Two-dimensional materials for highly efficient and stable perovskite solar cells. *Nano-Micro Lett.* **16**(1), 201 (2024). <https://doi.org/10.1007/s40820-024-01417-1>
10. K.T. Cho, G. Grancini, Y. Lee, E. Oveisi, J. Ryu et al., Selective growth of layered perovskites for stable and efficient photovoltaics. *Energy Environ. Sci.* **11**(4), 952–959 (2018). <https://doi.org/10.1039/c7ee03513f>
11. P. Liu, X. Li, T. Cai, W. Xing, N. Yang et al., Molecular structure tailoring of organic spacers for high-performance Ruddlesden-Popper perovskite solar cells. *Nano-Micro Lett.* **17**(1), 35 (2024). <https://doi.org/10.1007/s40820-024-01500-7>
12. S. Sidhik, Y. Wang, M. De Siena, R. Asadpour, A.J. Torma et al., Deterministic fabrication of 3D/2D perovskite bilayer stacks for durable and efficient solar cells. *Science* **377**(6613), 1425–1430 (2022). <https://doi.org/10.1126/science.abq7652>
13. X. Chang, R. Azmi, T. Yang, N. Wu, S.Y. Jeong et al., Solvent-dripping modulated 3D/2D heterostructures for high-performance perovskite solar cells. *Nat. Commun.* **16**(1), 1042 (2025). <https://doi.org/10.1038/s41467-025-56409-5>

14. M.-C. Shih, S. Tan, Y. Lu, T. Kodalle, D.-K. Lee et al., A 2D/3D heterostructure perovskite solar cell with a phase-pure and pristine 2D layer. *Adv. Mater.* **37**(17), 2416672 (2025). <https://doi.org/10.1002/adma.202416672>
15. P. Chen, D. He, X. Huang, C. Zhang, L. Wang, Bilayer 2D–3D perovskite heterostructures for efficient and stable solar cells. *ACS Nano* **18**(1), 67–88 (2024). <https://doi.org/10.1021/acsnano.3c09176>
16. L. Scaloni, Y. Vaynzof, Multidimensional perovskite solar cells: what's next after 3D/2D? *Adv. Energy Mater.* **15**(44), 2502686 (2025). <https://doi.org/10.1002/aenm.202502686>
17. Y. Zhang, C. Li, E. Bi, T. Wang, P. Zhang et al., Efficient inverted perovskite solar cells with a low-dimensional halide/perovskite heterostructure. *Adv. Energy Mater.* **12**(48), 2202191 (2022). <https://doi.org/10.1002/aenm.202202191>
18. D. Wang, J. Chen, P. Zhu, Y. Qiao, H. Hu et al., Binary microcrystal additives enabled antisolvent-free perovskite solar cells with high efficiency and stability. *Adv. Energy Mater.* **13**(7), 2203649 (2023). <https://doi.org/10.1002/aenm.202203649>
19. J. Wang, L. Liu, S. Chen, L. Qi, M. Zhao et al., Growth of 1D nanorod perovskite for surface passivation in FAPbI₃ perovskite solar cells. *Small* **18**(3), 2104100 (2022). <https://doi.org/10.1002/smll.202104100>
20. X. Chang, Y. Liu, Y. Ping, N. Wu, T. Yang et al., Multivalent ligands regulate dimensional engineering for inverted perovskite solar modules. *Science* **391**(6781), 153–159 (2026). <https://doi.org/10.1126/science.aea0656>
21. Y. Zou, Y. Zhao, Reconfiguring perovskite interlayers. *Nat. Mater.* **25**(2), 166–167 (2026). <https://doi.org/10.1038/s41563-025-02438-w>
22. T. Kong, H. Xie, Y. Zhang, J. Song, Y. Li et al., Perovskitoid-templated formation of a 1D@3D perovskite structure toward highly efficient and stable perovskite solar cells. *Adv. Energy Mater.* **11**(34), 2101018 (2021). <https://doi.org/10.1002/aenm.202101018>
23. S. Li, H. Gu, A. Zhu, J. Guo, C. Xi et al., Anion-cation synergistic regulation of low-dimensional perovskite passivation layer for perovskite solar cells. *Adv. Mater.* **37**(28), 2500988 (2025). <https://doi.org/10.1002/adma.202500988>
24. F. Wang, D. Duan, K. Zhou, Y.Z.B. Xue, X. Liang et al., Ionic liquid engineering enabled in-plane orientated 1D perovskite nanorods for efficient mixed-dimensional perovskite photovoltaics. *InfoMat* **5**(8), e12459 (2023). <https://doi.org/10.1002/inf2.12459>
25. F. Ye, T. Tian, J. Su, R. Jiang, J. Li et al., Tailoring low-dimensional perovskites passivation for efficient two-step-processed FAPbI₃ solar cells and modules. *Adv. Energy Mater.* **14**(4), 2302775 (2024). <https://doi.org/10.1002/aenm.202302775>
26. X. Zhou, X. Liang, F. Wang, H. Sun, Q. Zhu et al., Pyridine substitution strategy for one-dimensional perovskite: toward efficient and stable mixed-dimensional photovoltaics. *Chem. Eng. J.* **493**, 152539 (2024). <https://doi.org/10.1016/j.cej.2024.152539>
27. Y. Yang, H. Chen, C. Liu, J. Xu, C. Huang et al., Amidation of ligands for chemical and field-effect passivation stabilizes perovskite solar cells. *Science* **386**(6724), 898–902 (2024). <https://doi.org/10.1126/science.adr2091>
28. P. Shi, B. Ding, D. Jin, M. Oner, X. Zhang et al., Micro-homogeneity of lateral energy landscapes governs the performance in perovskite solar cells. *Nat. Commun.* **15**(1), 9703 (2024). <https://doi.org/10.1038/s41467-024-53953-4>
29. X. Zheng, S. Ahmed, Y. Zhang, G. Xu, J. Wang et al., Differentiating the 2D passivation from amorphous passivation in perovskite solar cells. *Nano-Micro Lett.* **18**(1), 62 (2025). <https://doi.org/10.1007/s40820-025-01913-y>
30. S. You, F.T. Eickemeyer, J. Gao, J.-H. Yum, X. Zheng et al., Bifunctional hole-shuttle molecule for improved interfacial energy level alignment and defect passivation in perovskite solar cells. *Nat. Energy* **8**(5), 515–525 (2023). <https://doi.org/10.1038/s41560-023-01249-0>
31. R.T. Ross, Some thermodynamics of photochemical systems. *J. Chem. Phys.* **46**(12), 4590–4593 (1967). <https://doi.org/10.1063/1.1840606>
32. C. Liu, Y. Yang, H. Chen, J. Xu, A. Liu et al., Bimolecularly passivated interface enables efficient and stable inverted perovskite solar cells. *Science* **382**(6672), 810–815 (2023). <https://doi.org/10.1126/science.adk1633>
33. H. Chen, A. Maxwell, C. Li, S. Teale, B. Chen et al., Regulating surface potential maximizes voltage in all-perovskite tandems. *Nature* **613**(7945), 676–681 (2023). <https://doi.org/10.1038/s41586-022-05541-z>
34. Y. Guo, F. Yao, Y. Zhang, G. Chen, S. Du et al., A universal surface fixed charge reconstruction strategy to minimize contact loss in wide bandgap perovskite photovoltaics. *Energy Environ. Sci.* **18**(10), 4916–4924 (2025). <https://doi.org/10.1039/D4EE05855K>
35. J. Wang, L. Zeng, D. Zhang, A. Maxwell, H. Chen et al., Halide homogenization for low energy loss in 2-eV-bandgap perovskites and increased efficiency in all-perovskite triple-junction solar cells. *Nat. Energy* **9**(1), 70–80 (2024). <https://doi.org/10.1038/s41560-023-01406-5>
36. Y. Zou, J. Liu, Y. Chang, C. Duan, W. Han et al., Differential ligand–cation interactions enable 2D-template-induced ordered assembly for efficient tin-based perovskite photovoltaics. *Adv. Mater.* **38**(12), e22717 (2026). <https://doi.org/10.1002/adma.202522717>
37. A. Diercks, J. Petry, T. Feeney, R. Singh, T. Zhao et al., Sequential evaporation of inverted FAPbI₃ perovskite solar cells—impact of substrate on crystallization and film formation. *ACS Energy Lett.* **10**(3), 1165–1173 (2025). <https://doi.org/10.1021/acseenergylett.4c03315>
38. B. Jiao, L. Tan, Y. Ye, N. Ren, M. Li et al., One-stone-two-birds: over 26% efficiency in perovskite solar cells *via* synergistic crystallization & interface regulation. *Energy Environ. Sci.* **18**(11), 5437–5447 (2025). <https://doi.org/10.1039/D5EE00189G>
39. H. Wang, S. Su, Y. Chen, M. Ren, S. Wang et al., Impurity-healing interface engineering for efficient perovskite submodules. *Nature* **634**(8036), 1091–1095 (2024). <https://doi.org/10.1038/s41586-024-08073-w>



40. Y. Zhao, F. Ma, Z. Qu, S. Yu, T. Shen et al., Inactive $(\text{PbI}_2)_2\text{RbCl}$ stabilizes perovskite films for efficient solar cells. *Science* **377**(6605), 531–534 (2022). <https://doi.org/10.1126/science.abp8873>
41. Y. Zou, W. Yu, H. Guo, Q. Li, X. Li et al., A crystal capping layer for formation of black-phase FAPbI₃ perovskite in humid air. *Science* **385**(6705), 161–167 (2024). <https://doi.org/10.1126/science.adn9646>
42. Y. Wen, T. Zhang, X. Wang, T. Liu, Y. Wang et al., Amorphous $(\text{lysine})_2\text{PbI}_2$ layer enhanced perovskite photovoltaics. *Nat. Commun.* **15**(1), 7085 (2024). <https://doi.org/10.1038/s41467-024-51551-y>
43. J. Wu, Y. Li, Y. Zhang, Y. Li, Y. Huang et al., Highly orientational order perovskite induced by in situ-generated 1D perovskitoid for efficient and stable printable photovoltaics. *Small* **18**(19), 2200130 (2022). <https://doi.org/10.1002/sml.202200130>
44. M. Lu, J. Ding, Q. Ma, Z. Zhang, M. Li et al., Dual-site passivation by heterocycle functionalized amidinium cations toward high-performance inverted perovskite solar cells and modules. *Energy Environ. Sci.* **18**(12), 5973–5984 (2025). <https://doi.org/10.1039/d5ee00524h>
45. L. Yang, Z. Fang, Y. Jin, H. Feng, B. Deng et al., Suppressing halide segregation *via* Pyridine-derivative isomers enables efficient 1.68 eV bandgap perovskite solar cells. *Adv. Mater.* **36**(21), 2311923 (2024). <https://doi.org/10.1002/adma.202311923>
46. Y. Xu, J. Yu, S. Liu, F. Tang, N. Ma et al., Surface potential homogenization improves perovskite solar cell performance. *Adv. Energy Mater.* **15**(12), 2404755 (2025). <https://doi.org/10.1002/aenm.202404755>
47. M. Li, J. Ding, Z. Zhang, Q. Ma, C. Li et al., Functional group engineering stabilizing precursor solution and passivating defects for operationally stable and highly reproducible inverted perovskite solar cells. *Adv. Mater.* **37**(27), 2502729 (2025). <https://doi.org/10.1002/adma.202502729>
48. H. Zheng, G. Liu, X. Dong, F. Chen, C. Wang et al., Self-regulated bilateral anchoring enables efficient charge transport pathways for high-performance rigid and flexible perovskite solar cells. *Nano-Micro Lett.* **17**(1), 328 (2025). <https://doi.org/10.1007/s40820-025-01846-6>
49. Y.-H. Huang, S.-Y. Zou, C.-Y. Sheng, Y.-C. Fang, X.-D. Wang et al., Lattice anchoring stabilizes α -FAPbI₃ perovskite for high-performance X-ray detectors. *Nano-Micro Lett.* **18**(1), 14 (2025). <https://doi.org/10.1007/s40820-025-01856-4>
50. H. Chen, S. Teale, B. Chen, Y. Hou, L. Grater et al., Quantum-size-tuned heterostructures enable efficient and stable inverted perovskite solar cells. *Nat. Photon.* **16**(5), 352–358 (2022). <https://doi.org/10.1038/s41566-022-00985-1>
51. Y. Liu, T. Ma, C. Wang, Z. Yang, Y. Zhao et al., Synergistic immobilization of ions in mixed tin-lead and all-perovskite tandem solar cells. *Nat. Commun.* **16**(1), 3477 (2025). <https://doi.org/10.1038/s41467-025-58810-6>
52. M. Stolterfoht, C.M. Wolff, J.A. Márquez, S. Zhang, C.J. Hages et al., Visualization and suppression of interfacial recombination for high-efficiency large-area pin perovskite solar cells. *Nat. Energy* **3**(10), 847–854 (2018). <https://doi.org/10.1038/s41560-018-0219-8>
53. S.D. Stranks, R.L.Z. Hoye, D. Di, R.H. Friend, F. Deschler, The physics of light emission in halide perovskite devices. *Adv. Mater.* **31**(47), 1803336 (2019). <https://doi.org/10.1002/adma.201803336>
54. J. Warby, F. Zu, S. Zeiske, E. Gutierrez-Partida, L. Frohloff et al., Understanding performance limiting interfacial recombination in pin perovskite solar cells. *Adv. Energy Mater.* **12**(12), 2103567 (2022). <https://doi.org/10.1002/aenm.202103567>
55. C. Geng, K. Zhang, C. Wang, C.H. Wu, J. Jiang et al., Crystallization modulation and holistic passivation enables efficient two-terminal perovskite/CuIn(Ga)Se₂ tandem solar cells. *Nano-Micro Lett.* **17**(1), 8 (2024). <https://doi.org/10.1007/s40820-024-01514-1>
56. X. Zang, S. Xiong, S. Jiang, D. Li, H. Wu et al., Passivating dipole layer bridged 3D/2D perovskite heterojunction for highly efficient and stable p-i-n solar cells. *Adv. Mater.* **36**(13), 2309991 (2024). <https://doi.org/10.1002/adma.202309991>
57. X. Zhang, F. Liu, Y. Guan, Y. Zou, C. Wu et al., Reducing the Voc loss of hole transport layer-free carbon-based perovskite solar cells *via* dual interfacial passivation. *Nano-Micro Lett.* **17**(1), 258 (2025). <https://doi.org/10.1007/s40820-025-01775-4>

Publisher's Note Springer Nature remains neutral with regard to jurisdictional claims in published maps and institutional affiliations.